JOURNAL OF NANOMATERIALS AND DEVICES
Jan - Jun 2026, VOL. 4, ISSUE 1, pp. 4 - 10
https://doi.org/10.61577/jnd.2026.100002

RESEAPRO JOURNALS

OPEN ACCESS

ORIGINAL ARTICLE

Phase-Dependent NO_2 gas-sensing performance of WO_3 nanostructures:An evidence-based quantitative re-analysis of published experimental data (2020–2025)

Sunny Sharma and Sultana Khatoon

Department of Applied Science, Phonics University, Roorkee, Uttarakhand, India

ABSTRACT

Metal-oxide chemiresistors often exhibit trade-offs among sensitivity, operating temperature, humidity tolerance, and recovery speed. This study provides a focused secondary quantitative re-analysis of published WO_3 NO_2-sensing data, centered on the open dataset. A common $WO_3{\cdot}H_2O$ precursor was converted at 200°C to monoclinic m-WO_3 (TF200) in a tubular furnace and cubic c-WO_3 (MF200) in a muffle furnace. Reported XRD, Raman, SEM, BET, optical, and gas-sensing results were re-examined without generating or imputing laboratory observations. m-WO_3 had a larger BET surface area (40.6 vs. 25.0 m^2 g^{-1}) and higher responses at 0.25, 0.50, 1.0, and 2.5 ppm NO_2 (116, 366, 1061, and 1322 vs. 83, 183, 511, and 780). Exploratory regressions based on only four published concentration-level means per phase (n = 4) gave linear R^2 values of 0.797 and 0.912 and power-law R^2 values of 0.895 and 0.953 for m-WO_3 and c-WO_3, respectively. Because raw replicate-level measurements were unavailable, these fits and their p-values are descriptive and exploratory rather than confirmatory statistical inference. At 2.5 ppm, response times were 239 s for m-WO_3 and 204 s for c-WO_3. Overall, the published dataset shows phase-dependent trade-offs among surface area, response magnitude, detection limit, and response/recovery kinetics.

KEY WORDS

WO_3; Tungsten trioxide; Nanostructures; NO_2 sensor; Chemiresistive sensing; Oxygen vacancies; Gas sensing

ARTICLE HISTORY

Received 6 February 2026;
Revised 22 February 2026;
Accepted 02 March 2026

Introduction

Nitrogen dioxide is a combustion-related pollutant and an important target for distributed environmental monitoring. Chemiresistive metal-oxide sensors are compact, comparatively inexpensive, and readily integrated with microheaters and interdigitated electrodes (IDEs). Among commonly investigated metal oxides, WO_3 is highly responsive to oxidizing gases. Its sensing behavior is not determined by composition alone: crystal phase, film porosity, exposed facets, grain boundaries, oxygen-vacancy chemistry, and operating temperature influence the density and electronic behavior of adsorption sites [1,2].

Accordingly, recent WO_3 research has increasingly focused on engineering the structure-property-sensing relationship rather than on synthesis alone. Highly porous flame-aerosol WO_3 films showed that increasing film thickness from 0.5 to 12.3 µm can change the NO_2 response by more than an order of magnitude [3]. Surface engineering, p-n heterojunctions, noble-metal decoration, transition-metal doping, and WO_3/MXene composites have all been investigated to enhance responses to low-concentration oxidizing gases or to lower operating temperature [4-9]. However, response definitions, humidity, gas concentration, and thermal conditions remain heterogeneous across studies, while photoactivation offers one route to reduce the required thermal energy [10].

This paper does not generate or impute laboratory observations. Instead, it provides a focused secondary analysis of a published paired-material dataset in which a common precursor and sensing protocol were used, while the calcination environment produced different WO_3 phases surface areas, and pore structures. The aims were to summarize the reported synthesis and characterization, compare NO_2 concentration-response behavior, examine response/recovery kinetics and repeatability, and contextualize the reported theoretical detection limits. The paired design is useful for highlighting phase- and surface-related trade-offs without implying that either phase is universally superior (Figure 1).

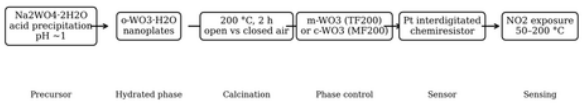


Figure 1. Analytical workflow linking precursor preparation, phase-controlled calcination, sensor fabrication, and NO_2 sensing. Original schematic prepared for this manuscript from the workflow reported by Do et al.; no source graphical material is reproduced [11].

Materials and Methods

Evidence base and study design

This study provides a secondary quantitative re-analysis and includes no new laboratory experiments. The primary evidence is the open-access report of Do et al., which describes WO_3 nanoplates using XRD, Raman spectroscopy, SEM, BET analysis, UV-visible characterization, and chemiresistive sensing [11]. Throughout this manuscript, TF200 denotes monoclinic m-WO_3 and MF200 denotes cubic c-WO_3.

***Correspondence:** Mr. Sunny Sharma, Department of Applied Science, Phonics University, Roorkee, Uttarakhand, India. e-mail: s9797sharma@gmail.com
© 2026 The Author(s). Published by Reseapro Journals. This is an Open Access article distributed under the terms of the Creative Commons Attribution License (http://creativecommons.org/licenses/by/4.0/), which permits unrestricted use, distribution, and reproduction in any medium, provided the original work is properly cited.

Peer-reviewed studies from 2020-2025 are used only for contextual benchmarking where response definitions and experimental conditions permit meaningful comparison [12-16].

Materials and synthesis

For the core experiment, WO_3 nanoplates were prepared by acid precipitation from $Na_2WO_4{\cdot}2H_2O$. Nitric acid was used to adjust the medium to approximately pH 1, promoting formation of tungstic acid and subsequent orthorhombic $WO_3{\cdot}H_2O$. The common precursor was then calcined for 2 h at 200°C. Heating in an open tubular furnace produced monoclinic m-WO_3 (TF200), whereas the more enclosed muffle-furnace environment produced cubic c-WO_3 (MF200). Because precursor chemistry and nominal calcination conditions were held constant, the paired system provides a useful basis for phase-dependent comparison (Table 1) [11].

Sensor fabrication and measurement

The reported sensor paste contained 20 mg of WO_3 powder dispersed in 1 mL of dimethylformamide. A 0.5 µL aliquot was drop-coated onto a SiO_2 substrate with interdigitated Pt electrodes, dried at 80 °C, and then heat-treated at 200 °C for 2 h. Resistance was measured with a Keithley 2602A source meter, while gas flow was controlled by mass-flow controllers. Following Do et al., sensor response was defined as S = Rg/Ra, where Rg is the resistance in the target gas and Ra is the resistance in air [11].

Characterization variables

Phase assignment used the reported XRD peak positions and Raman bands. Crystallite size is commonly estimated using $D = K\lambda/(\beta\cos\theta)$, where D is the coherent crystallite dimension, K is the shape factor, λ is the X-ray wavelength, β is peak broadening in radians, and θ is the Bragg angle. Because the required peak-width values were not available in the published numerical dataset, no Scherrer crystallite size was calculated. Morphological dimensions were taken from the reported SEM analysis, while BET surface area, mean pore diameter, pore volume, and optical band gap were retained as published.

Statistical analysis

Concentration-response analysis used the four published concentration-level means for each phase at 0.25, 0.50, 1.0, and 2.5 ppm NO_2. Summary statistics included the mean, sample standard deviation, range, and coefficient of variation across these four concentration levels; these quantities describe the response series and do not estimate device-to-device variability. Exploratory calibration models included a linear form ($S = a + bC$) and a power-law form ($S = aC^b$), with the latter fitted after log transformation. Slopes, R^2 values, two-sided regression p-values, and residual standard errors were calculated as descriptive diagnostics. Because raw replicate-level responses were unavailable, ANOVA, Tukey comparisons, replicate-derived confidence intervals, and fabricated error bars were not used. Thus, all regression statistics are exploratory and should not be interpreted as confirmatory inference.

Table 1. Core synthesis and phase-control conditions reported by Do et al. [11].

Sample	Starting material	Transformation	Environment	Final phase	Key purpose
Precursor	$Na_2WO_4{\cdot}2H_2O$	Acid precipitation, pH ≈1	Room temperature	o-$WO_3{\cdot}H_2O$	Common hydrated precursor
c-WO_3 (MF200)	$WO_3{\cdot}H_2O$	200 °C, 2 h	Closed muffle furnace	c-WO_3	Cubic comparison phase
m-WO_3 (TF200)	$WO_3{\cdot}H_2O$	200 °C, 2 h	Open tubular furnace	m-WO_3	Monoclinic comparison phase

Note. No hydrothermal synthesis was substituted for the core experiment; the source used acid precipitation followed by controlled calcination.

Results

Structural, morphological and surface characterization

Orthorhombic $WO_3{\cdot}H_2O$ served as the common precursor. After calcination, c-WO_3 (MF200) showed reported reflections at 23.9°, 33.98°, 49.25°, 55.25°, and 61.07°, assigned to the (100), (110), (111), (200), and (211) planes, respectively, with a reported lattice constant of 3.84 Å. m-WO_3 (TF200) showed reflections in the same general region at approximately 23.1°, 23.7°, 24.2°, 34.1°, 49°, 56°, and 62°, with no reported secondary-phase peaks. Raman bands further distinguished the cubic phase (approximately 266, 676, and 821 cm^{-1}, with a higher-order feature near 940 cm^{-1}) from the monoclinic phase (273, 717, and 810 cm^{-1}) (Table 2; Figures 2 and 3) [11].

Table 2. Structural, morphological, surface and optical properties of the core WO_3 materials.

Material	Phase	Approx. size (nm)	BET ($m^2\ g^{-1}$)	Pore dia. (nm)	Pore vol. ($cm^3\ g^{-1}$)	Band gap (eV)
$WO_3{\cdot}H_2O$	Orthorhombic	Nano plates	20.8	25.0	0.136	2.39
c-WO_3 (MF200)	Cubic	250×200×40	25.0	19.1	0.146	2.51
m-WO_3 (TF200)	Monoclinic	200×200×30	40.6	13.8	0.178	2.69

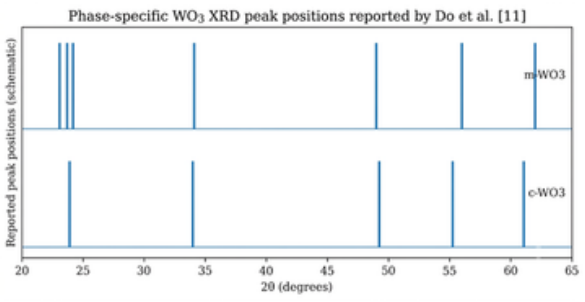


Figure 2. Phase-specific XRD peak positions for c-WO_3 (MF200) and m-WO_3 (TF200). Original schematic prepared for this manuscript from peak positions reported by Do et al.; no source diffraction intensities or graphical material are reproduced [11].

© Reseapro Journals 2026
https://doi.org/10.61577/jnd.2026.100002

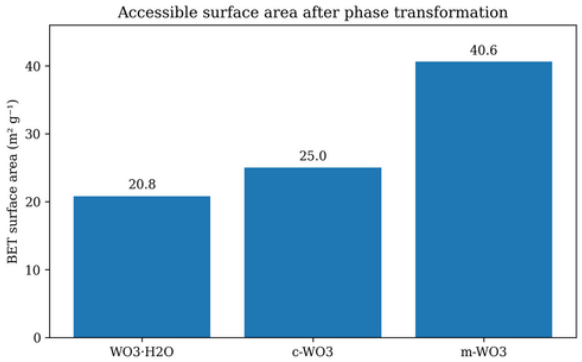


Figure 3. BET surface-area comparison for the hydrated precursor, c-WO_3 (MF200), and m-WO_3 (TF200). Original chart prepared for this manuscript from numerical values reported by Do et al.; no source graphical material is reproduced [11].

Morphology and surface characteristics

SEM showed plate-like particles of approximately 250 × 200 × 40 nm for c-WO_3 (MF200) and 200 × 200 × 30 nm for m-WO_3 (TF200). The clearest contrast was in accessible surface structure. BET surface area increased from 20.8 m^2 g^{-1} in the hydrated precursor to 25.0 m^2 g^{-1} for c-WO_3 and 40.6 m^2 g^{-1} for m-WO_3. Mean pore diameter decreased from 25.0 nm in the precursor to 19.1 nm and 13.8 nm in c-WO_3 and m-WO_3, respectively, while pore volume increased from 0.136 to 0.146 and 0.178 cm^3 g^{-1}, respectively. Reported optical band gaps were 2.39 eV for the precursor, 2.51 eV for c-WO_3, and 2.69 eV for m-WO_3. Together, these values indicate that the phase transformation was accompanied by substantial changes in surface area and pore structure, particularly for the monoclinic material.

NO_2 Response and Concentration

At 150°C, m-WO_3 (TF200) showed responses of 116, 366, 1061, and 1322 at 0.25, 0.50, 1.0, and 2.5 ppm NO_2, respectively, compared with 83, 183, 511, and 780 for c-WO_3 (MF200). The corresponding response advantage of m-WO_3 over c-WO_3 was 39.8%, 100.0%, 107.6%, and 69.5%. Across the four concentration levels, the mean ± sample SD was 716.3 ± 568.3 for m-WO_3 and 389.3 ± 318.2 for c-WO_3. The large coefficients of variation (79.3% and 81.8%, respectively) reflect the deliberately increasing concentration series and should not be interpreted as experimental or device-level variability (Table 3; Figures 4 and 5).

Table 3. NO_2 concentration-response data at 150 °C and derived phase advantage.

NO_2 (ppm)	m-WO_3 (TF200) response	c-WO_3 (MF200) response	m-WO_3 advantage (%)
0.25	116	83	39.8
0.5	366	183	100.0
1	1016	511	107.6
2.5	1322	780	69.5
Mean ± sample SD	716.3 ± 568.3	389.3 ± 318.2	-

Note. SD summarizes variability across the four concentration-level responses and is not a replicate-sensor standard deviation.

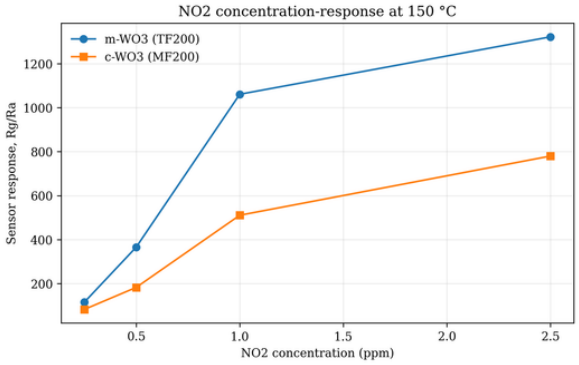


Figure 4. Concentration-dependent NO_2 response of m-WO_3 (TF200) and c-WO_3 (MF200) at 150 °C. Original chart prepared for this manuscript from published numerical values in Do et al.; no error bars are shown because replicate-level values were unavailable, and no source graphical material is reproduced [11].

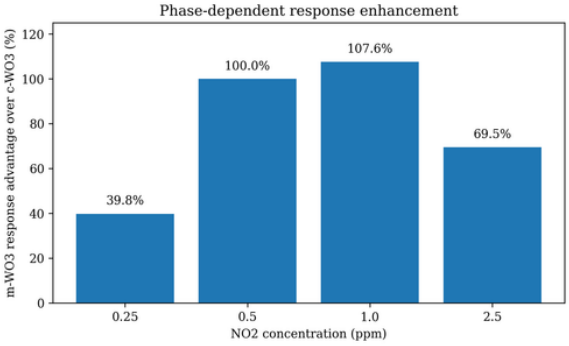


Figure 5. Percentage increase in m-WO_3 (TF200) response relative to c-WO_3 (MF200) at each reported NO_2 concentration. Original chart prepared for this manuscript from the published numerical values; no source graphical material is reproduced.

Regression analysis

Linear fits to the four published concentration-level means (n = 4 per phase) gave S = 181.34 + 503.45C for m-WO_3 (R^2 = 0.797, p = 0.1072) and S = 68.80 + 301.60C for c-WO_3 (R^2 = 0.912, p = 0.0449). The corresponding residual standard errors were 313.5 and 115.5 response units. Power-law fits estimated after log transformation were $S = 675.08C^{1.074}$ for m-WO_3 (R^2 = 0.895, p = 0.0540) and $S = 373.49C^{1.004}$ for c-WO_3 (R^2 = 0.953, p = 0.0239), with log-scale residual standard errors of 0.444 and 0.269, respectively. Because only four published concentration means were available and no replicate-level observations were provided, these fitted parameters and p-values are exploratory descriptors of response shape and must not be interpreted as confirmatory statistical inference (Table 4).

Table 4. Exploratory concentration-response regression statistics.

Phase	Linear equation	Linear R^2	Linear p	Power-law equation	Power-law R^2 (p)
m-WO_3 (TF200)	181.34 + 503.45C	0.797	0.1072	675.08C^ 1.074	0.895 (0.0540)
c-WO_3 (MF200)	68.80 + 301.60C	0.912	0.0449	373.49C^ 1.004	0.953 (0.0239)

© Reseapro Journals 2026
https://doi.org/10.61577/jnd.2026.100002

Note. n = 4 published concentration-level means per phase; raw replicate-level responses were unavailable. Reported p-values and fitted parameters are exploratory descriptors, not confirmatory inference. Linear-model RSE: 313.5 (m-WO_3) and 115.5 (c-WO_3); log-scale power-law RSE: 0.444 and 0.269, respectively.

Operating temperature, kinetics, selectivity and repeatability

Both phases were evaluated over the reported 50-200°C operating range, with 150 °C treated as the empirical optimum in the source study [11]. At 150 °C and 2.5 ppm NO_2, m-WO_3 (TF200) required 239 s to respond and 77 s to recover, whereas c-WO_3 (MF200) required 204 s and 47 s, respectively. Thus, m-WO_3 combined the larger response with a 17.2% longer response time and a 63.8% longer recovery time than c-WO_3. The paired results therefore illustrate a sensitivity-kinetics trade-off rather than a single performance metric that favors one phase under all conditions (Figure 6).

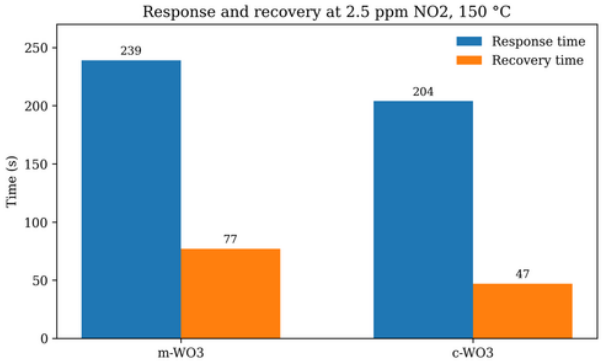


Figure 6. Response and recovery times of m-WO_3 (TF200) and c-WO_3 (MF200) at 2.5 ppm NO_2 and 150 °C. Original chart prepared for this manuscript from numerical values reported by Do et al.; no source graphical material is reproduced [11].

Repeatability, selectivity and detection limit

The source study examined five repeated exposures to 1 ppm NO_2 and reported reproducible transients, but cycle-specific numerical values were not provided. Accordingly, no replicate standard deviation was reconstructed. Both phases were also reported to show strong preference for 2.5 ppm NO_2 over substantially higher concentrations of H_2, ethanol, NH_3, and H_2S. Because exact interferent-response magnitudes were not available as numerical data, a selectivity ratio was not calculated. The reported theoretical detection limits were 0.10 ppb for m-WO_3 (TF200) and 0.05 ppb for c-WO_3 (MF200), while the cubic phase also showed the faster response/recovery kinetics under the reported optimum condition (Table 5).

Benchmarking against recent WO_3 sensors

Recent literature shows that WO_3 response can be enhanced through several material-engineering pathways, although direct comparisons require attention to gas concentration, temperature, humidity, and response definition. Layered WO_3 showed a response of 106 to 5 ppm NO_2 with a reported LOD of 0.243 ppb at 160 °C [17]. A $WO_3/Ti_3C_2T_x$ composite showed a response of 78 to 200 ppb NO_2 at room temperature with 182/75 s response/recovery times [7]. Electrospun WO_3 nanofibers showed a response of 12.523 at 1 ppm and 200 °C with 11/26 s kinetics, whereas a ZnO/WO_3 flower heterostructure showed a response of 5.9 at 100 ppb and 190 °C with 7/9 s kinetics [18,19]. Ni-doped WO_3 showed a response of 396 with 13/6 s kinetics and a reported 510 ppt detection limit at 160 °C, while Co-doped WO_3 showed a 20,776% response at 10 ppm with 15/23 s kinetics [8,20]. Porous sol-gel films detected NO_2 down to 80 ppb, and hydrothermal or defect-engineered variants further demonstrate morphology-dependent tuning (Table 6; Figure 7) [16,21-24].

Table 5. Core sensing-performance summary at the reported optimum temperature.

Phase	Optimum T	Response @2.5 ppm	Response time	Recovery time	Theoretical LOD	Repeatability / selectivity
m-WO_3 (TF200)	150 °C	1322	239 s	77 s	0.10 ppb	5 cycles reported; strong NO_2 preference
c-WO_3 (MF200)	150 °C	780	204 s	47 s	0.05 ppb	5 cycles reported; strong NO_2 preference

Note. Exact numerical interferent responses and cycle-level repeatability values were not available as machine-readable data and were not reconstructed from graphical bars.

Table 6. Selected 2020–2025 WO_3-based NO_2 sensor benchmarks. Response magnitudes are not pooled because definitions differ among studies.

Study/material	NO_2 condition	Operating T	Reported response	Resp./rec. time	LOD / note
Do et al., m-WO_3 (TF200) [11]	2.5 ppm	150 °C	1322 (Rg/Ra)	239/77 s	0.10 ppb (theoretical)
Do et al., c-WO_3 (MF200)	2.5 ppm	150 °C	780 (Rg/Ra)	204/47 s	0.05 ppb (theoretical)
Wang & Ansari, layered WO_3 [17]	5 ppm	160 °C	106	—	0.243 ppb
Gasso & Mahajan WO_3/MXene [7]	0.2 ppm	Room T	78	182/75 s	ppb-range

© Reseapro Journals 2026
https://doi.org/10.61577/jnd.2026.100002

Qiu & Wang, nanofibers [18]	1 ppm	200 °C	12.523	11/26 s	—
Wei et al., ZnO/WO_3 [19]	0.1 ppm	190 °C	5.9	7/9 s	low-conc. heterojunction
Liu et al., Ni-WO_3 [8]	reported test	160 °C	396	13/6 s	510 ppt
Kumar et al., Co-WO_3 [20]	10 ppm	200 °C	20,776%	15/23 s	95% stability at 8 weeks
Rani et al., nanosheets [23]	50 ppm	150 °C	38%	85/315 s	1 ppm
Morais et al., microflowers [24]	5 ppm	150 °C	225	14.5/2.4 min	65 ppb

Note. "—" indicates that a directly comparable value was not used. Different response definitions and gas concentrations preclude direct ranking by response magnitude.

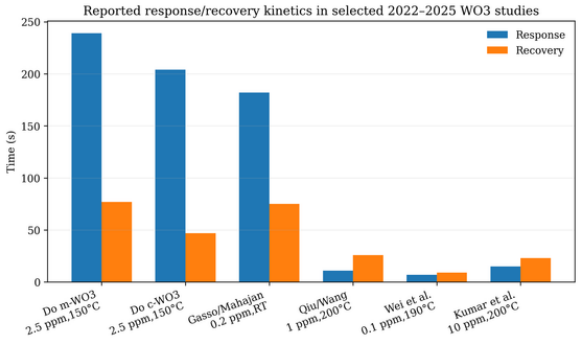


Figure 7. Reported response/recovery kinetics for selected WO_3-based NO_2 sensors. Original comparative chart prepared for this manuscript from numerical values cited in Table 6; test concentrations and temperatures differ, the chart compares kinetics only, and no source graphical material is reproduced.

Discussion

The core dataset illustrates a clear structure-property-sensing association within the paired WO_3 system. Both materials were calcined at the same nominal temperature for the same duration, but different furnace environments produced different crystal phases and pore structures. m-WO_3 (TF200) had a BET surface area 62.4% higher than c-WO_3 (MF200) (40.6 vs. 25.0 $m^2\ g^{-1}$). The larger NO_2 response of m-WO_3 is therefore consistent with its greater accessible surface area, smaller mean pore diameter, and larger pore volume, all of which can increase gas-solid contact and the number of available adsorption sites. Phase-dependent defects may further modify adsorption and charge-transfer energetics; however, the published paired dataset supports association rather than a definitive causal partitioning of these individual mechanisms.

NO_2 gas-sensing mechanism

In air, n-type WO_3 interacts with adsorbed oxygen species that withdraw conduction electrons and increase resistance, represented schematically by $O_2(g) \rightarrow O_2(ads)$ and $O_2(ads) + e^- \rightarrow O_2^-(ads)$. NO_2 is a strong electron acceptor and can further withdraw electrons through adsorption and surface-reaction pathways, increasing the resistance response. The literature also indicates that phase-dependent defects and oxygen-vacancy populations can alter adsorption capacity and charge transfer. This provides a mechanistic basis for sensor-performance changes produced by Ni, Co, and Al incorporation or Au decoration [8,9,25].

Temperature, kinetics, and device engineering

The reported optimum near 150 °C reflects competing adsorption, reaction, and desorption kinetics. At low temperature, adsorption may occur while surface reactions and desorption remain slow; increasing temperature can accelerate charge transfer and clear occupied sites. At excessively high temperature, shorter adsorbate residence times can reduce surface coverage. Accordingly, a larger steady-state response does not necessarily imply faster recovery. In the paired dataset, c-WO_3 (MF200) showed faster response/recovery and a lower reported theoretical LOD, whereas m-WO_3 (TF200) showed the larger response. The preferred material therefore depends on application priorities: rapid alarm sensing may emphasize speed and detection threshold, while analytical monitoring may place greater weight on response magnitude. Device engineering, including charge-storage or heterostructure strategies, can further alter these trade-offs even at low operating temperatures [13,14].

Humidity and practical implications

Humidity remains an important constraint for practical deployment. Ghosh et al. reduced humidity-dependent variation in a 3 ppm WO_3 NO_2 sensor through physicochemical and flow optimization [12]. $WO_3/Ti_3C_2T_x$ systems have also been developed for room-temperature operation with improved humidity tolerance [6]. Pulsed-laser-deposited WO_3 films provide another route to low-temperature sensing through control of oxygen-vacancy-related film properties [15]. Consequently, claims of NO_2 selectivity should be interpreted together with operating temperature, humidity, interferent concentrations, and the response definition used.

Limitations and future research

Several limitations define the scope of this analysis. First, the regressions use only four published concentration-level means per phase rather than raw replicate-level observations; their p-values, residual errors, and fitted parameters are therefore exploratory and cannot support confirmatory inference. Second, response definitions and test conditions differ across benchmarking studies, which prevents quantitative pooling. Third, exact selectivity and repeatability values were not available as machine-readable numerical data and were not reconstructed from graphical bars. Future studies would benefit from machine-readable raw data, humidity-resolved calibration, long-term stability testing, device-to-device replication, uncertainty estimates, and standardized response definitions. Without such information, formal meta-analysis and robust cross-study uncertainty quantification remain limited.

© Reseapro Journals 2026
https://doi.org/10.61577/jnd.2026.100002

Conclusion

This study provides a focused comparative secondary summary of the phase-dependent NO_2-sensing behavior reported for paired WO_3 nanoplates prepared from a common precursor. In the published dataset, m-WO_3 (TF200) had the larger BET surface area (40.6 m^2 g^{-1}) and a higher response at 2.5 ppm NO_2 (1322 vs. 780), whereas c-WO_3 (MF200) showed faster response/recovery (204/47 s vs. 239/77 s) and the lower reported theoretical detection limit (0.05 vs. 0.10 ppb). The linear and power-law fits reported here were calculated from only four published concentration-level means per phase (n = 4). Because raw replicate-level measurements were unavailable, the resulting p-values, residual errors, and fitted parameters are exploratory descriptors rather than confirmatory statistical evidence. Accordingly, the present work should be interpreted as a focused comparative synthesis of the published dataset rather than as a deep independent re-analysis. Together with the 2020-2025 literature, the evidence highlights phase- and surface-dependent trade-offs among response magnitude, kinetics, operating temperature, and detection limit, supporting the use of phase and surface engineering to tune WO_3-based NO_2 sensors for application-specific requirements.

Conflict of Interest

The author(s) declare that they have no known competing financial interests or personal relationships that could have appeared to influence the work reported in this manuscript.

Funding Statement

This research received no specific grant from any funding agency in the public, commercial or not-for-profit sectors.

Acknowledgements

The author(s) acknowledge the institutional support and library resources made available during the preparation of this review.

References

1. Staerz A, Somacescu S, Epifani M, Kida T, Weimar U, Barsan N. WO3-based gas sensors: Identifying inherent qualities and understanding the sensing mechanism. ACS sensors. 2020;5(6):1624-1633. https://doi.org/10.1021/acssensors.0c00113
2. Li X, Fu L, Karimi-Maleh H, Chen F, Zhao S. Innovations in WO3 gas sensors: Nanostructure engineering, functionalization, and future perspectives. Heliyon. 2024;10(6):e27740. https://doi.org/10.1016/j.heliyon.2024.e27740
3. Abegg S, Klein Cerrejon D, Güntner AT, Pratsinis SE. Thickness optimization of highly porous flame-aerosol deposited WO3 films for NO2 sensing at ppb. Nanomaterials. 2020;10(6):1170. https://doi.org/10.3390/nano10061170
4. Drmosh QA, Al Wajih YA, Al-Rammah R, Qamar M, Yamani ZH. Surface-engineered WO3 thin films for efficient NO2 sensing. Appl Surf Sci. 2020;517:146235. https://doi.org/10.1016/j.apsusc.2020.146235
5. He W, Zhao Y, Xiong Y. Bilayer polyaniline-WO3 thin-film sensors sensitive to NO2. ACS omega. 2020;5(17):9744-9751. https://doi.org/10.1021/acsomega.9b04122
6. Gasso S, Mahajan A. Development of highly sensitive and humidity independent room temperature NO2 gas sensor using two-dimensional Ti3C2T x Nanosheets and one dimensional WO3 nanorods nanocomposite. ACS sensors. 2022;7(8):2454-2464. https://doi.org/10.1021/acssensors.2c01213
7. Gasso S, Mahajan A. MXene decorated tungsten trioxide nanocomposite-based sensor capable of detecting NO2 gas down to ppb-level at room temperature. Mater Sci Semicond Process. 2022;152:107048. https://doi.org/10.1016/j.mssp.2022.107048
8. Liu F, Song H, Wu L, Zhao J, Yao X, Fu K, et al. Excellent NO2 gas sensor based on the oxygen inhibiting effect of Ni3+-doped WO3. Colloids Surf A: Physicochem Eng Asp. 2023;666:131329. https://doi.org/10.1016/j.colsurfa.2023.131329
9. Wang Q, Li R, Wang P, Zhang Y, Wang Y, Yang Y, et al. Au-decorated WO3-based sensor for chemiresistive detection of NO2 at 80° C. Sens Actuators B: Chem. 2023;390:133985. https://doi.org/10.1016/j.snb.2023.133985
10. Šetka M, Claros M, Chmela O, Vallejos S. Photoactivated materials and sensors for NO2 monitoring. J Mater Chem C. 2021;9(47):16804-16827. https://doi.org/10.1039/D1TC04247E
11. Do DT, Nguyen DY, Pham TA, Nguyen CT, Nguyen VH. Comparative study of monoclinic and cubic WO3 nanoplates on NO2 gas-sensing properties. RSC Advances. 2025;15(28):22930-22940. https://doi.org/10.1039/D5RA01820J
12. Ghosh S, Ilango MS, Prajapati CS, Bhat N. Reduction of humidity effect in WO3 thin film-based NO2 sensor using physiochemical optimization. Cryst Res Technol. 2021;56(1):2000155. https://doi.org/10.1002/crat.202000155
13. Shin W, Hong S, Jeong Y, Jung G, Park J, Kim D, et al. Effect of charge storage engineering on the NO2 gas sensing properties of a WO3 FET-type gas sensor with a horizontal floating-gate. Nanoscale. 2021;13(19):9009-9017. https://doi.org/10.1039/D1NR00513H
14. Bian W, Dou H, Wang X, Li C, Zhang Y, Gong C, et al. Fabrication and computational study of a chemiresistive NO2 gas sensor based on the carbon dots-WO3 heterostructure for operating below room temperature. ACS sensors. 2023;8(2):748-756. https://doi.org/10.1021/acssensors.2c02291
15. Bellucci A, De Bonis A, Curcio M, Santagata A, Pace ML, Bolli E, et al. WO3-based thin films grown by pulsed laser deposition as gas sensors for NO2 detection. Sensors. 2024;24(22):7366. https://doi.org/10.3390/s24227366
16. Wan Z, Ge C, Bai L, Hussain S, Liu G, Qiao G, et al. Sol-gel-derived WO3 thin films with structure-dependent NO2 sensing properties. Ceram Int. 2024;50(19):36900-36907. https://doi.org/10.1016/j.ceramint.2024.07.077
17. Wang X, Ansari D. Superior sensitivity and low detection limit of NO2 sensor based on layered tungsten oxide. J Environ Chem Eng. 2022;10(3):107786. https://doi.org/10.1016/j.jece.2022.107786
18. Qiu Y, Wang Y. Synthesis, growth kinetics and ultra-sensitive performance of electrospun WO3 nanofibers for NO2 detection. Appl Surf Sci. 2023;608:155112. https://doi.org/10.1016/j.apsusc.2022.155112
19. Wei S, Chang G, Liu Y, Wu Y, Zhang Y, Hu Y, et al. Heterojunction and exposed facet engineering of ZnO/WO3 flower structure for fast and sensitive low-concentration NO2 sensing. Mater Res Bull. 2023;163:112218. https://doi.org/10.1016/j.materresbull.2023.112218

© Reseapro Journals 2026
https://doi.org/10.61577/jnd.2026.100002

20. Kumar DK, Bharathi P, Archana J, Navaneethan M, Harish S. Optimizing NO2 gas sensor performance: Investigating the influence of cobalt doping on WO3 recovery kinetics for enhanced gas sensing application. Sens Actuators B: Chem. 2024;421:136477. https://doi.org/10.1016/j.snb.2024.136477
21. Mathankumar G, Bharathi P, Archana J, Harish S, Navaneethan M. Defect manipulation of WO3 nanostructures by yttrium for ultra-sensitive and highly selective NO2 detection. Sens Actuators B: Chem. 2022;353:131057. https://doi.org/10.1016/j.snb.2021.131057
22. Hingangavkar GM, Navale YH, Nimbalkar TM, Mulik RN, Patil VB. Hydrothermally engineered WO3 nanoflowers: A selective detection towards toxic NO2 gas. Sens Actuators B: Chem. 2022;371:132584. https://doi.org/10.1016/j.snb.2022.132584
23. Rani S, Dahiya R, Kumar V, Berwal P, Sihag S. Hydrothermally engineered WO3 nanosheets as potential NO2 gas sensor. Ionics. 2025;31(1):993-1002. https://doi.org/10.1007/s11581-024-05934-2
24. Morais PV, Suman PH, Orlandi MO. NO2 detection using hierarchical WO3 microflower-based gas sensors: comprehensive study of sensor performance. Chemosensors. 2025;13(11):390. https://doi.org/10.3390/chemosensors13110390
25. Devender KK, Palanisamy B, Jayaram A, Mani N, Santhana Krishnan H. Transition metal-engineered oxygen vacancy-mediated Al-doped WO3 nanoplates for NO2 detection. ACS Appl Nano Mater. 2025;8(1):65-79. https://doi.org/10.1021/acsanm.4c04634

© Reseapro Journals 2026
https://doi.org/10.61577/jnd.2026.100002